Adaptive mesh interface capturing for cavitating compressible flows using Discontinuous Galerkin discretisation.

Andreas Papoutsakis*[,1], Phoevos Koukouvinis [1], Manolis Gavaises [1]
[1] School of Mathematics, Computer Science and Engineering, Department of Mechanical Engineering and Aeronautics, EC1V 0HB, London, UK
*Corresponding author: andreas.papoutsakis@city.ac.uk

Abstract
In this work we use an implementation of the Discontinuous Galerkin (DG) method which features on-the-fly adaptive mesh refinement for unstructured hybrid meshes for the modelling of cavitating two-phase flows. The specific implementation has been developed for the resolution of complex multiscale phenomena, where high accuracy p-adaptive discretisations are combined with an h-adaptive data structure. The suggested approach accommodates the fine spatial resolution of the interface discontinuities in a cavitating flow.
The physical problem of a cavitating flow is modelled by the simple barotropic model, as a unified compressible working fluid. The governing equations consist of the transport equations for the conservation of mass and momentum. Pressure is calculated explicitly from the density distribution using the a piece-wise equation of state (EoS). The Tait EoS is used for the saturated liquid and an isentropic approximation is used for evaluation of the vapour-liquid mixture pressure. Scope of this work is to obtain a high order discretisation for the conservation of mass and momentum, to accurately describe the flow structures responsible for the formation of cavitation bubbles, and the capturing of the resulting shocks during bubble collapse.
The numerical approach is assessed for a series of test cases of compressible two-phase flows. Specifically, the one-dimensional shock tube problem for the advancement of a compressible interface front and the symmetric bubble collapse problem are considered. Furthermore, the axisymmetric bubble collapse near a wall is also presented. The method is applied for the Large Eddy Simulation (LES) in a micro-channel flow used for the study of the effects of cavitation on liquid jet atomisation.

Keywords
Cavitation; Adaptive Mesh refinement; Barotropic model; Discontinuous Galerkin Method; Atomisation;

Introduction

Cavitation is observed in a variety of engineering applications such as turbomachinery [2], injectors [3, 4, 5, 6, 7, 8], hydrofoils and propulsion systems [9]. The performance of devices subject to cavitation is affected due to the vaporisation of the liquid phase. Cavitation induces vibrations, noise [10] and limits the performance characteristics of hydrodynamic machines [11]. The solid material confining cavitating flows is subject to cavitation erosion [12], induced by the subsequent collapse of the vapour bubbles. Besides the above-mentioned unfavourable consequences of cavitation in engineering applications, there are cases where cavitation is desirable. Droplet atomisation is enhanced by cavitation in injector nozzles [3, 7, 13]. In surface treatment applications, the erosive characteristics of collapsing bubbles are employed [9].
Bubbles exhibit a unique feature by focusing the potential energy of the surrounding pressure field during their collapse, to a small scale. Examples of this function is the delivery of a micro-scale impinging jet during the collapse of bubbles [14] or the increase of the temperature of the contained vapour [15]. The applicability of this property of bubbles has been investigated by numerous studies. The prospect of using cavitating bubbles as micro-scale chemical reactors is investigated in [15]. A review of novel applications of cavitating flows in the field of bio-engineering is presented on [16]. Bubbly flows appear *in vivo* [17] in living organisms and they are used for enhancing the depicting potential of ultrasound imaging [18]. The focusing characteristics of collapsing bubbles provide a promising method in delivering micro-scale incisions for injecting macro-molecules like genes or enzymes [19] into cells and cellular organs, for thrombolysis micro-operations [20], and for targeted drug delivery [21]. The scales of these phenomena in biological systems vary from the sub-cellular scale within the cytoplasm [17] and the cytoplasmic membrane of a cell, up to the level of a whole tissue as in the applications of lithotripsy, histotripsy, thromvolysis and histectomy [16].
An experimental setup that advocates the investigation of the mechanisms responsible for the onset of cavitation is the throttled micro-channel configuration [7, 6]. Modelling approaches to the problem of cavitation in injectors and channels incorporate a variety of turbulent models ranging from Reynolds Averaged Navier-Stokes models (RANS)[3] to Large Eddy Simulations (LES) [33] and fully resolved Direct Numerical Simulations (DNS) [54]. In the LES framework the Smagorinsky model (SM) [8] and the Coherent Structure Model (CSM) [55] have been incorporated for the cases of injector flows and for hydrofoil simulations. In [34], the WALE variation has been applied, accounting for the effect of the wall. Finally, in [8] and in [5, 33] the Adaptive Local Deconvolution (ADLM) model [56] is suggested.
The Discontinuous Galerkin method [22, 23, 24, 25] combines high order accuracy with the ability to handle complex geometries described by hybrid unstructured meshes. The computational efficiency of this method (alongside the

spectral volume [24, 26] and spectral difference [24, 27, 28] methods), however, is generally believed to be inferior to more commonly used methods, such as the Finite Differences (FD) and Finite Volume (FV) [29, 30] methods. The Finite Volume methodology (FV) remains the most popular approach to descretising the governing equations for cavitating flows, either in a pressure based framework [4, 3], or in a density based approach [31, 32, 5, 33, 34]. Recently DG has been used for the modelling of compressible cavitating flows, [35, 36]. In the work of [35, 36] the Modified Ghost Fluid Method (MGFM) [37, 35] was used for the treatment of the interface between the liquid and vapour phases in an explosion induced cavitating flow near a deformable wall. In the same equation the Tait EoS was used for the liquid phase alongside a cutoff cavitating model for the liquid/vapour mixture. In [51] a genuinely DG implementation of the Kapila five equation model is presented and assessed for one-dimensional problems. In [52] DG is used for the modelling of cavitating flows where filtering, MINMOD limiting on the conservative space, and the HLLC approximate Riemann solver are employed for the solution of one dimensional problems.
In this work we use the high-order ForestDG implementation of the Discontinuous Galerkin method which features on-the-fly adaptive mesh refinement for unstructured hybrid meshes. The specific implementation has been developed for the resolution of complex multiscale phenomena where high accuracy p-adaptive discretisations are combined with an h-adaptive data structure which accommodates the fine spatial resolution aiming to minimise the discrepancies stemming form the resolution of the interface discontinuities [43].
In the following section we present the governing equations and the numerical discretisation of the modelling approach for compressible two-phase flows used in our analysis. In the results section, the method is assessed for one- and two-dimensional compressible two-phase flow problems. In the same section, the method is used for the investigation of the flow in a throttled micro-channel flow.

Material and methods

The compressible formulation of the Navier-Stokes equations is used for the modelling of the working fluid. The flow field is described by the Eulerian state vector field $\mathbf{U}(\mathbf{x},t)$, and consists of the density ρ, and the momentum vector $\rho\mathbf{u}$ fields at $\mathbf{x}$, t. For the general case of a viscous turbulent flow field which is modelled in the LES context the Favre averaging operator $\widetilde{(\cdot)} = \overline{\rho(\cdot)}/\overline{\rho}$ is used for the filtering of the small turbulent scales. The Favre averaged state vector is defined as $\widetilde{\mathbf{U}}(\mathbf{x},t) = (\overline{\rho}, \overline{\rho}\widetilde{u}_1, \overline{\rho}\widetilde{u}_2, \overline{\rho}\widetilde{u}_3)$ and reduces to the instantaneous state vector $\mathbf{U}$ for laminar or fully resolved simulations. The conservation of the mass and momentum provide the set of the governing equations for the turbulent compressible flow of the working fluid. The strong conservative form for $\widetilde{\mathbf{U}}$ can be presented as [44]:

$$\frac{\partial \widetilde{\mathbf{U}}}{dt} + \nabla \cdot \mathbf{f}_{inv}\left(\widetilde{\mathbf{U}}\right) - \frac{1}{\mathrm{Re}}\nabla \cdot \mathbf{f}_{vis}\left(\widetilde{\mathbf{U}}, \widetilde{\mathbf{\Theta}}\right) = S\left(\widetilde{\mathbf{U}}\right) \ , \tag{1}$$

$$\widetilde{\mathbf{\Theta}} = \nabla \mathbf{f}_{aux}\left(\widetilde{\mathbf{U}}\right) \ . \tag{2}$$

The source term $S\left(\mathbf{U}\right) = (-2/r)\mathbf{U}$ accounts for the transformation of the domain to spherical coordinates. $\mathbf{f}_{inv}$ is the 4×3 tensor of the inviscid fluxes and $\mathbf{f}_{vis}$ is the 4×3 tensor for the viscous fluxes and are defined as:

$$\mathbf{f}_{inv} = \begin{bmatrix} \overline{\rho}\widetilde{u}_j \\ \overline{\rho}\widetilde{u}_i\widetilde{u}_j + \overline{p}\delta_{i,j} \end{bmatrix}, \ \mathbf{f}_{vis} = \begin{bmatrix} 0 \\ 2\left(\mu + \mu_t\right) S^*_{i,j} \end{bmatrix}, \ \mathbf{f}_{aux} = \begin{bmatrix} \widetilde{u}_i \end{bmatrix} \ , \tag{3}$$

$S^*_{ij} = \frac{1}{2}\left(\frac{\partial \widetilde{u}_j}{\partial x_i} + \frac{\partial \widetilde{u}_i}{\partial x_j}\right) - \frac{1}{3}\delta_{ij}\frac{\partial \widetilde{u}_k}{\partial x_k}$ is the traceless rate of strain tensor related to the viscous stress tensor $\tau_{ij} = 2\mu S^*_{ij}$, the non-dimensional local viscosity μ is normalised by the dynamic viscosity at the reference temperature. The auxiliary state vector $\widetilde{\mathbf{\Theta}}$ contains the spatial gradients of the 3×1 auxiliary flux $\mathbf{f}_{aux}$ for the diffusive components of the state vector $\widetilde{\mathbf{U}}$ as defined in Equation (2). $\widetilde{\mathbf{\Theta}}$ is used for the evaluation of the viscous fluxes $\mathbf{f}_{vis}$. The Wall Adapting Local Eddy viscosity model (WALE) [53] is used for the evaluation of the normalised turbulent viscosity μ_t. Assuming that Re is defined for the reference dynamic viscosity μ_0 used for the normalisation of μ, the turbulent viscosity μ_t is provided by the following expression of the WALE model:

$$\mu_t = \left(\frac{\overline{\rho}\Delta^2 C_w^2}{\mu_0}\right) \frac{\left(\widetilde{S}^d_{ij}\widetilde{S}^d_{ij}\right)^{3/2}}{\left(\widetilde{S}_{ij}\widetilde{S}_{ij}\right)^{5/2} + \left(\widetilde{S}^d_{ij}\widetilde{S}^d_{ij}\right)^{5/4}} \ , \tag{4}$$

with $\widetilde{S}^d_{ij} = \frac{1}{2}\left(\widetilde{g^2}_{ij} + \widetilde{g^2}_{ji}\right) + \delta_{ij}\widetilde{g^2}_{kk}$, $\widetilde{S}_{ij} = \frac{1}{2}\left(\frac{\partial u_i}{\partial x_j} + \frac{\partial u_j}{\partial x_i}\right)$, where $\widetilde{g^2}_{ij}$ is defined as $\widetilde{g^2}_{ij} = \widetilde{g}_{ik}\widetilde{g}_{kj}$ and $\widetilde{g}_{ij} = \frac{\partial \widetilde{u}_i}{\partial x_j}$.
The auxiliary variables vector $\widetilde{\mathbf{\Theta}}$ is discretised separately resulting in three equations for each one of the diffusive components of the state vector. Equations (1) and (2) comprise the coupled formulation of the governing equations for $\widetilde{\mathbf{X}} = \left[\widetilde{\mathbf{U}}, \widetilde{\mathbf{\Theta}}\right]$ for a turbulent compressible two-phase flow.
The piece-wise barotropic Equation of State (EoS) is used for the modelling of the fluid subject to cavitation as in [31, 5]. In this approach the liquid phase is modelled by the Tait EoS where the thermal effects are not taken into account, thus assuming constant temperature. This allows for the modelling of compression waves in the

Table 1. Properties of the EoS for working fluids presented in our analyses.

Fluid	B (Pa)	n	$\rho_{\mathrm{sat},l}$ (kg/m^3)	C (Pa · kg/m^3)	p_{sat} (Pa)
Water	$293.5 \cdot 10^6$	7.15	998.2	1450	2339
Diesel fuel	$181.4 \cdot 10^6$	7.15	830.0	1250	4500

liquid phase without solving for the energy equation. The vapour/liquid mixture is again modelled assuming that the mixture follows an isentropic path [5]. The interface between the pure liquid and the liquid/vapour mixture is described by the density distribution and is identified by the $\rho = \rho_{sat,l}$ iso-surface. For turbulent flows the complex interaction between the interface and the small unresolved scales of the velocity field is considered to take place at a low Weber number regime which is expected to dampen the unresolved interface fluctuations.
The EoS provides an explicit expression for the pressure of the working fluid, as a function of the density. The Tait equation of state is used for densities larger than the saturation density ρ_{sat}. For smaller densities, the working fluid is a mixture of liquid and vapour and its pressure is provided by the second branch of the piece-wise EoS, which based on a local equilibrium assumption where the mixture is following an isentropic path. The piecewise state equation is then provided by the following equation:

$$p = \begin{cases} p_{sat} + B\left(\left(\frac{\rho}{\rho_{sat}}\right)^n - 1\right) & \rho \geq \rho_{sat,l} \\ p_{sat} + C\left(\frac{1}{\rho_{sat}} - \frac{1}{\rho}\right) & \rho < \rho_{sat,l} \end{cases} . \tag{5}$$

The Tait EoS branch in Equation (5) B is the bulk modulus of the liquid, and the exponent n is taken equal to 7.15. In the isentropic EoS for the mixture C is a constant characteristic of the fluid material and independent of the temperature. The values $p_{sat,l}$ and $p_{sat,v}$ correspond to the pressure of the liquid and the gaseous phase at the saturation point. Also $\rho_{sat,l}$ and $\rho_{sat,v}$ are the densities of the saturated liquid and the saturation gas. The speed of sound for the liquid/vapour system is provided by the square root of first derivative of the pressure $\sqrt{dp/d\rho}$ and exhibits a discontinuity at ρ_{sat}:

$$c = \begin{cases} \sqrt{Bn\frac{\rho^{n-1}}{\rho^n_{sat,l}}} & \rho \geq \rho_{sat,l} \\ \sqrt{\frac{C}{\rho^2}} & \rho < \rho_{sat} \end{cases} \tag{6}$$

In the analyses presented, we investigate cavitating flows for water and for Diesel fuel as in the throttled microchannel configuration of [34]. The parameters of the these working fluids are presented in Table 1. The variation of the pressure and the speed of sound as a function of the liquid/vapour mixture is shown in the Figures 1(**Left**) and 1(**Right**), respectively.

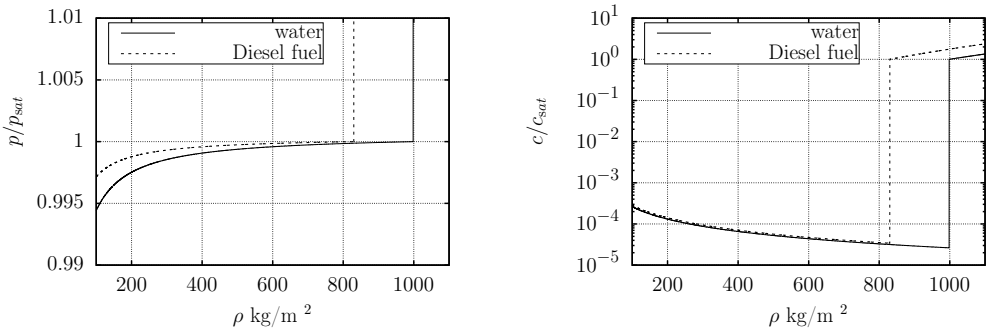

Figure 1. Left Variation of pressure with density. **Right** Variation of the speed of sound with density. Solid curves corresponds to water with $\rho_{sat} = 998.2$kg/m^3, and $c_{\mathrm{sat}} = 1450$m/s, dashed curves correspond to Diesel fuel with $\rho_{sat} = 830.0$kg/m^3 and $c_{\mathrm{sat}} = 1250$m/s [45, 8].

The computational domain Ω is discretised into N unstructured elements E_m ($\Omega = \cup E_m$). A weak formulation of the governing equations is obtained by multiplying the conservative formulation with a test function $w(\mathbf{x})$ and integrating them over the element. In the Galerkin context, the test function is taken from the same set of polynomial basis functions used for the interpolation of the state vector $\mathbf{U}$ and the extended state vector $\mathbf{X}$. The interpolated distribution $\mathbf{U}_h^m$ for $\mathbf{U}$ is defined as the weighted sum of the N_p polynomial basis functions, as:

$$\mathbf{U}_h^m = \sum_{i=1}^{N_p} \mathbf{c}_i^m(t) b_i(\mathbf{x}) \text{ , for } m = 1, N_p \text{ ,} \tag{7}$$

where p is the maximum degree of the interpolation. In this expansion, the coefficients $\mathbf{c}_i(t)$ constitute the degrees of freedom of the solution. $b_i(\mathbf{x})$ is the tensor product of the Legendre polynomial basis functions in the three spatial dimensions. The integral formulation of the governing Equations (1) is expressed as:

$$\int_{E_m} b_i \frac{\partial \mathbf{U}_h^m}{\partial t} dE + \oint_{S_m} b_i \mathbf{f}\left(\mathbf{X}_h^m\right) \cdot \mathbf{n} dS - \int_{E_m} \nabla b_i \cdot \mathbf{f}\left(\mathbf{X}_h^m\right) dE = \int_{E_m} b_i \mathbf{w}_d^m dE \quad \text{for} \quad i = 1, N_p,\ m = 1, N\ , \tag{8}$$

providing a set of $N_p \times N$ equations for $\mathbf{c}_i^m(t)$. The volume and surface integrals in Equation (8) are defined in the physical space. The integrals are evaluated in the transformed domain for the computational space elements using the Gauss-Legendre quadrature rule and the Jacobian of the transformation [47] of the physical coordinates for each element of the discretisation E_m to the computational space Ω_m of the FEM element.
The surface integrals are defined on the surface of the element $S_m = \partial E_m$ and are calculated in the computational space, with $\mathbf{n}$ defined as the outward normal unit vector. In the weak formulation presented in Equation (8), the flux $\mathbf{f}$ represents the viscous and inviscid fluxes in Equation (1) as $\mathbf{f} = \mathbf{F}_{inv} + \frac{1}{\mathrm{Re}}\mathbf{F}_{vis}$. The continuity of the interpolated variables across the element faces is not required in the DG context, thus, the values of the approximations on each side of the face S_m, $\mathbf{U}_h^{m(-)}$ and $\mathbf{U}_h^{m(+)}$ are doubly defined. The evaluation of the fluxes at the boundaries of the elements is a function of $\mathbf{U}_h^{m(-)}$ and $\mathbf{U}_h^{m(+)}$, and it is common for the adjoin elements ensuring the conservativeness of the discretisation scheme.
For the Local Lax-Friedrichs (LLF) scheme the inviscid fluxes $\mathbf{F}_{inv}$ are evaluated from the mean value of the variables on the two face sides $\{\mathbf{U}_h^m\}$, where an artificial diffusion term, proportional to the jump of the fluxes on the bounding surface $[[\mathbf{U}_h^m]]$, is introduced via the equation:

$$\mathbf{F}_{inv} = \mathbf{F}_{inv}\left(\{\mathbf{U}_h^m\}\right) + \frac{\lambda_i}{2}[[\mathbf{U}_h^m]]\ , \tag{9}$$

where, in the LLF scheme, $\lambda_i = \max\left(|F'_{inv}(U_i)|\right)$ is the maximum absolute eigenvalue of the inviscid flux at the specific position of the interface (Local). For the standard Lax-Friedrichs (LF) scheme the global maximum of the absolute eigenvalue in the whole domain is used instead.
In addition to the LF and the LLF schemes, the hybrid [46] and the HLLC [48] schemes have been implemented for a simple one dimensional realisation (RKDG) of the discontinuous Galerkin method which was used for the derivation of the test case simulations presented in the next section. The time-advancement for both the 3D AMR and the 1D RKDG implementations is based on the non-oscillatory 3rd order RK algorithm of [49].
In the current DG implementation, the capturing of the different length-scales of the vapour-liquid interface, the flow vortical structure and the resulting compression waves are modelled using the the h/p-refinement characteristics of the ForestDG implementation described in [43]. This approach results in non-conformal faces between the neighbouring adapted elements. The evaluation of the fluxes across the non-conformalities is addressed by ensuring the conservativeness of the discretisation as described in [41].
The on-the-fly AMR implementation used, allows for the continuous refinement and coarsening of the grid. Thus, it presents shock capturing characteristics and enhances the resolution of the interface discontinuities. It proves as a powerful tool for modelling the complex mechanism of bubble growth due to coherent vortical structures in the flow, the volatile topology of the bubble interface during bubble collapse and the capturing of the pressure wave fronts generated by the bubble collapse. A limiting approach, however, is still necessary to detect and smooth sharp gradients by limiting the fluxes at the interfaces where the local gradients exceed the solution of the neighbouring elements, thus preserving the monotonicity of the solution. For this a MINMOD limiting approach in the space of the conservative variables is used [52].

Results and discussion

In this work the implementation of the DG methodology for the solution of the barotropic model is used for the simulation of the turbulent cavitating flow through the throttled slit injector geometry, described in [34]. The working fluid is Diesel. Before moving on to the application simulations we first present a series of test cases in order to validate the DG implementation. The problems of this family are inviscid, fully resolved simulations for one- and two-dimensional configurations with water as a working liquid. The details of all the cases simulated in this work are summarised in the Table 2.

One dimensional problems

For `CaseA`, we consider a a liquid-vapour interface in an one dimensional configuration. The material constants B and n for the equation of state (5) are taken equal to $B = 293.526643 \cdot 10^6\mathrm{Pa}$ and $n = 7.15$. The liquid density at the saturation point is $\rho_{sat} = \rho_{l,sat} = 998.2\mathrm{kg/s}$. The computational domain extends along the x-axis from $x = -L/2$ to $x = L/2$. The domain is split into a left (L) interval $[-L/2, 0]$ and a right (R) interval $[0, L/2]$. The total length of the computational domain is $L = 40.0m$ and is discretised with $N = 1000\ p1$ elements. The left side (L) is initialised as liquid water at with $\rho_L = 1000\mathrm{kg}/m^3$ and is considered quiescent ($U_L = 0m/s$), the right side (R) is initialised as a vapour/liquid mixture with $\rho_R = 0.001\rho_{sat,l}$ moving at a speed of $U_L = 0.3c$.
The distribution of the non-dimensionalised velocity for `CaseA` at $t = 0.01$sec, is shown in the Figure 2(**Left**). In this figure we show the result of the one-dimensional implementation RKDG for the barotropic model using various approximate Riemann solvers, identified by the coloured curves in the diagram. Specifically, we present the result

Table 2. Operating conditions for the simulations presented. The subscripts $high$ and low correspond to the left and right values (L,R) for the initialisation of the shock tube problem. For the bubble collapse cases they correspond to the values outside and inside the bubble. For the throttled injector case $high$ refers to the inlet boundary condition and low to the outlet condition.

Case	`CaseA`	`CaseB`	`CaseC`	`CaseD`
Setup	Shock tube	Symmetric bubble	Near wall bubble	Micro channel
Fluid	Water	Water	Water	Diesel
ρ_{high}	1000 kg/m^3	998.246 kg/m^3	1002.89 kg/m^3	847.9 kg/m^3
ρ_{low}	0.998 kg/m^3	8.851kg/m^3	49.41kg/m^3	837.4kg/m
p_{high}	38.1 bar	1.0 bar	100.0 bar	300 bar
p_{low}	887.8 Pa	2176.7 Pa	2311.5 Pa	120bar
u_{high}	0	0	0	N/A
u_{low}	$0.3c_{\text{sat},l}$	0	0	N/A

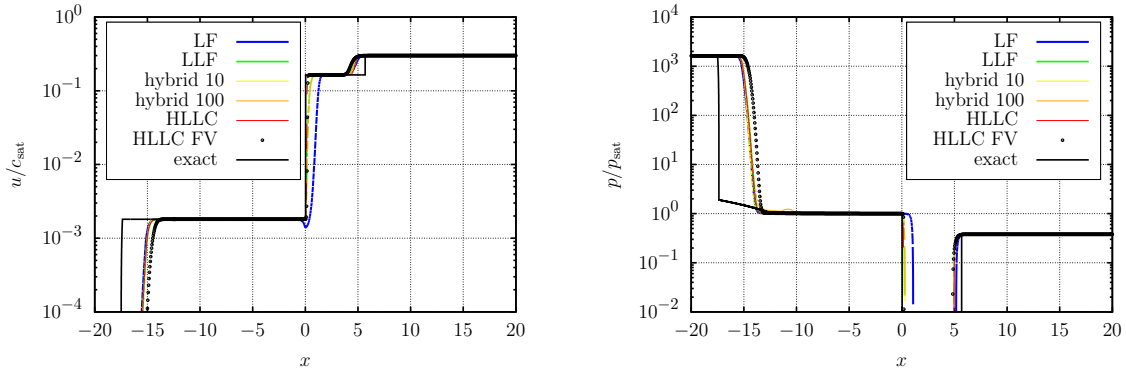

Figure 2. Left: Distribution of non-dimensional velocity, for the shock tube problem `CaseA` at $t = 0.01s$. **Right:** Distribution of non-dimensional pressure for the shock tube problem `CaseA` at $t = 0.01s$.

for the LF, the LLF, the hybrid scheme with $\alpha = 10$ and with $\alpha = 100$ and finally the result from the HLLC scheme. In the same figure we present the Finite Volume (FV) solution with the HLLC scheme represented with dots and the exact solution of the Riemann problem represented by the a black curve. The flow exhibits two shock waves, (L and R), and the interface discontinuity, which has propagated by ~ 0.02m to the right. At the instance presented in the Figure 2(**Left**) the L wave is located at $x \sim -17.5$m and the R wave is located near $x \sim 5.5$m.
By comparing the numerical solutions obtained with FV and DG to the exact solution we can see that apart from the LF approach all methods provide a satisfactory solution of the problem, by capturing the discontinuities both at the shocks and on the interface. The HLLC scheme provides the sharpest capturing of the interface both for the FV and the DG implementation. For the L and R shocks, however the LLF and the hybrid solvers provide similar result. For the L and R shocks the FV approach seems to lag compared to the DG implementations.
The result for the classic Rayleigh-Plecet symmetric bubble collapse problem [14, 50, 31] is presented in the Figure 3. The collapse time T [14] assuming incompressibility for the liquid phase is provided by the Rayleigh equation for the bubble radius. The collapse time T is obtained by integrating the Rayleigh equation:

$$\dot{R} = -\sqrt{\frac{2}{3}\frac{p_\infty - p_v}{\rho}\left[\frac{R_0^3}{R^3} - 1\right]}, \; T = 0.915 R_0 \sqrt{\frac{\rho_l}{p_\infty - p_v}}, \tag{10}$$

where R_0 is the initial bubble radius, p_∞ is the pressure of the surrounding liquid, p_v is the pressure of the vapour, and ρ_l is the density of the liquid. For the parameters of the problem `caseB` as provided in the table 2, $T = 92.5\mu$sec or $T = 134.13 L_0/c_{\text{sat},l}$. The problem is solved with the one-dimensional RKDG implementation and the spherical symmetry is accounted by the source term S in Equation (1). In the Figure 3(**Left**) we present the temporal evolution of the bubble radius as inferred from the RKDG solver, for the different discretisation schemes compared with the theoretical result from the integration of the Equation (10). The LLF the hybrid and the HLLC solvers give the same result which is close to the theoretical result inferred by the equation 10. In Figure 3(**Right**) we present the result for the radial velocity of the collapsing bubble at $t = 0.9692T$ which corresponds to a bubble radius $R = 0.28R_0$.

Bubble colapse near wall

Four characteristic instances from the solution of the near wall bubble collapse problem are depicted in the Figure 4. For this specific case, (`CaseC`), we assume a low pressure vapour bubble cavity with $R = 0.4$mm which is located 16μm off a solid wall. The details of this setup are presented in the Table 1. The mesh is essentially unstructured and consists of prismatic and hexahedral elements forming a cylindrical wedge of 2^o that extends to $100R_0$ along the axis of symmetry and to $100R_0$ in the radial direction. During the simulation the mesh is refined, depending on

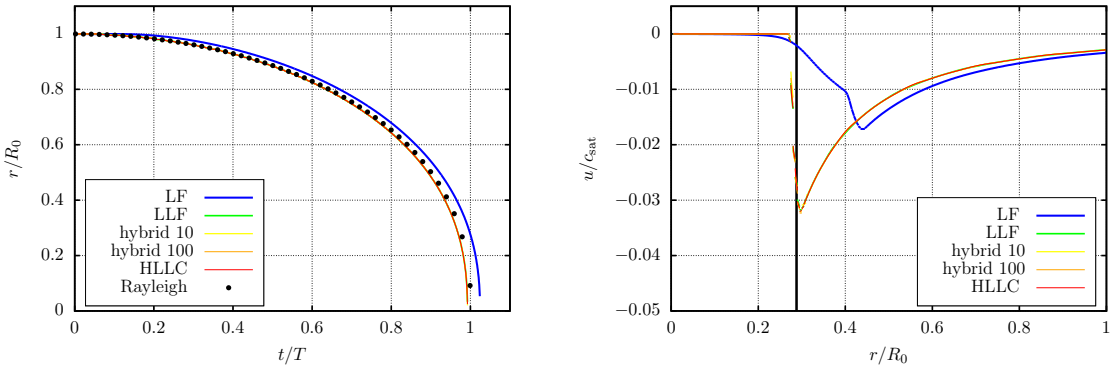

Figure 3. Left: Temporal evolution of the position of the bubble interface for the symmetrical bubble collapse problem `CaseB`, comparison with the Rayleigh collapse curve. **Right:** Distribution of non-dimensional velocity at $t = 0.9692T$. The black solid line corresponds to the theoretical result for the position of the interface at this instance ($R = 0.28R_0$).

the density gradient magnitude, reaching to up to four levels at the vapour liquid interface. In addition, the mesh is refined in areas of high vorticity to up to three levels in two dimensions using a quad-tree topology.

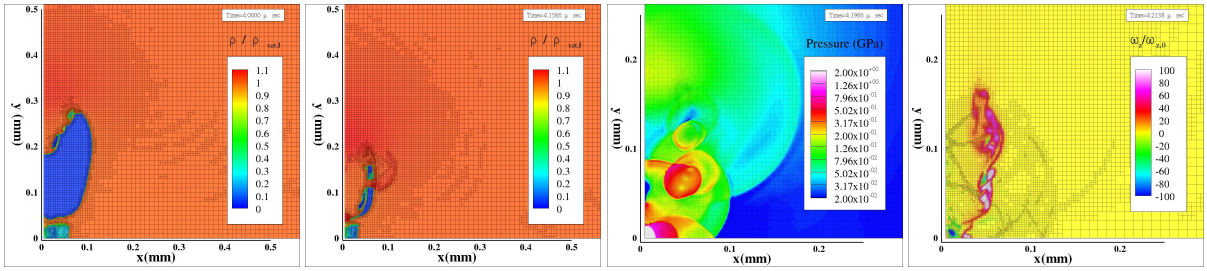

(**a**) (**b**) (**c**) (**d**)

Figure 4. (**a**),(**b**):Density distribution for `CaseC`. An impingement jet forms at the top of the bubble which later penetrates the bubble resulting in its collapse (**c**):Pressure distribution after the collapse of the bubble identifying multiple localities of collapse. (**d**): Vorticity distribution after the collapse of the bubble during the impingement of the jet on the wall. The jet is identified by the vortical structures formed at the vicinity of the shear layer of the jet.

Large Eddy Simulation in a microchannel

In the Figure 5 we present the computational setup for the throttled micro-channel flow for the configuration described in [34]. The micro-channel is characterised by a cross-section 0.3mm$\times 0.3$mm on the $y-z$ plane and extends for 1mm on the x-direction. The inlet and outlet geometry configurations are sharp (I-inlet and outlet) with negligible curvature. The inlet and outlet pressures are 300bar and 120bar, respectively and the working fluid for this simulation is Diesel fuel. The material constants B and n for the equation of state (5) are taken equal to $B = 181.4 \cdot 10^6$Pa and $n = 7.15$ as presented in the Table 1. The liquid density at the saturation point is $\rho_{sat} = \rho_{l,sat} = 830.0$kg/s and the saturation pressure is 4500Pa. The computational mesh consists of a hybrid mesh of prismatic and hexahedral elements. The background mesh of 450.000 cells has been further adapted to 2 and 3 levels in all three dimensions, using an oct-tree topology.

In the Figure 5 we also present the density isorurface for $\rho = 0.9\rho_{sat,l}$ which identifies the location of the interface between the liquid phase and the liquid/vapour mixture. In the Figure 6(**Left**) we present the density distribution at an x-y slice of the domain located at z=0.15mm. The LES result for the u component of the velocity is presented in the Figure 6(**Right**) and is compared with the experimental result of [34] for the position $M2$, ie at $x = 0.6$mm.

Conclusions

A methodology for the modelling of cavitating flows that combines the high order characteristics of the Discontinuous Galerkin method with the adaptive resolution of the mesh for the resolution of the interface discontinuity was presented. The liquid and vapour phases are modelled in a unified approach based on the barotropic model, where a piece-wise equation of state is employed. The methodology was assessed through a series of test cases of compressible two-phase flows where different approximate Riemann solvers are used and have been compared with the FV implementation and theoretical solutions. The method was used for the investigation of the axisymmetric bubble collapse near a wall. The multi-scale modelling AMR approach which was used, revealed a complex collapse mechanism. We focused in the vortical structures induced by the impingement jet and the resolution of the distributed collapse of the bubble at multiple localities. The penetration of the bubble results to a rich spatial structure of shock waves, interacting with the auxiliary bubbles. The refinement of the computational mesh on shocks results

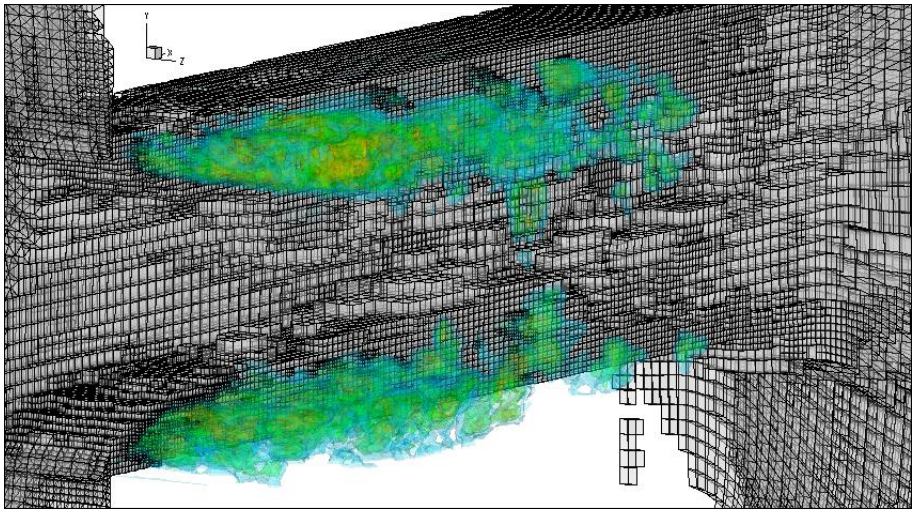

Figure 5. Iso-surface of the vapor mass fraction. Only the elements corresponding to high vorticity are shown. Cells with high vorticity are refined to a level equal to two, elements on the bubble interface are identified by the density gradient and are refined to a level equal to three.

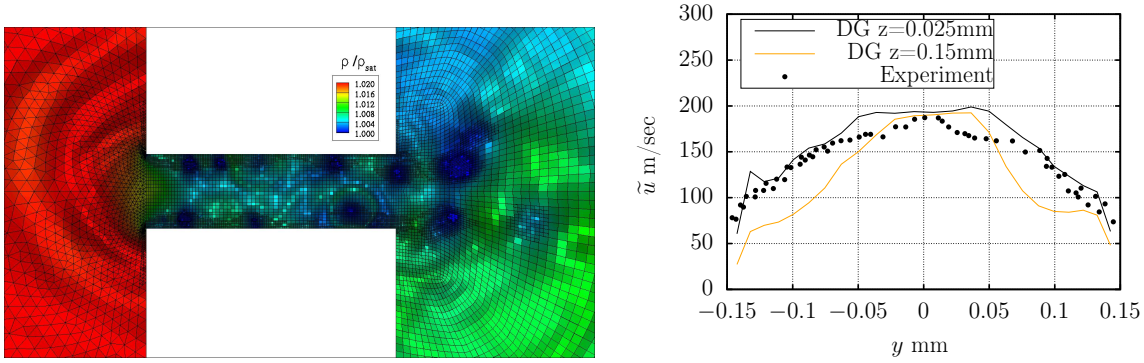

Figure 6. Large Eddy Simulation of the throttled flow experiment described in [34] (**Left**): Density distribution as a fraction of the saturation density of the liquid phase. Shadows identify the density gradients. (**Right**): Distribution of the Favre average of the x component of the velocity vector at the cross-section $x = 0.6mm$ along the y-axis. The values correspond to a the averaged values from $z = 0.00$mm up to $z = 0.05$mm.

in the resolution of the pressure gradients induced by the bubble collapse. The impact of the shock waves with the confining wall result to intense gradients on the interface which are expected to induce strong shear stresses on the wall material. The suggested approach was implemented for the modelling of a three-dimensional cavitating flow in a throttled micro-channel. For this case the effects of viscosity were accounted and the turbulent flowfield was modelled in the LES context using the WALE model for the eddy viscosity.

Acknowledgements

Nomenclature

B	bulk coefficient [Pa]
c	speed of sound [m s^{-1}]
$\mathbf{f}$	flux [N/A]
n	EoS exponent [-]
P	pressure [Pa]
Re	Reynolds number [-]
S	stress tensor [m s^{-2}]
$\mathbf{U}$	state vector [N/A]
Δ	filter width [m]
$\mathbf{\Theta}$	auxiliary vector [N/A]
μ	dynamic viscosity [kg m^{-3}]
ρ	density [kg m^{-1} s^{-1}]

References

[1] Koukouvinis, Ph., and Gavaises M., and Georgoulas, A., and Marengo, M., 2016, *Int. J. of Comput. Fluid Mech.*, pp. 1061–257.
[2] R. E. Arndt, 2002, *Ann. Rev. of Fluid Mech.* 34 (1), pp. 143–175.
[3] A. Giannadakis, K. Perrakis, T. Panidis, 2008, *Exp. Therm. Fluid Sci.*, 32 (8),pp. 1548–1563.
[4] E. Giannadakis, M. Gavaises, C. Arcoumanis, 2008, *J. Fluid Mech.*, 616, pp. 153–193.
[5] C. P. Egerer, S. Hickel, S. J. Schmidt, N. A. Adams, 2014, *Phys. Fluids*, 26 (8), 085102.
[6] R. Skoda, R. Schilling, M. T. Schobeiri, 2007, *Int. J. Rotating Mach.*, pp. 1–11.
[7] A. Sou, S. Hosokawa, A. Tomiyama, 2007,*Int. J. Heat Mass Transf.* 50 (17-18), pp. 3575–3582.
[8] W. Edelbauer, J. Strucl, A. Morozov, 2014, Adv. Hydroinformatics SIMHYDRO.
[9] R. E. ARNDT, 1981, "Recent Advances in Cavitation Research" Vol. 12, ACADEMIC PRESS, INC.
[10] B. Maines, R. E. A. Arndt, 1997, *Fluids Engng.*, 119 (2), pp. 271–276.
[11] J. X. Lu, S. Q. Yuan, J. P. Yuan, X. D. Ren, J. Pei, Q. R. Si, 2015, *J. Phys. Conf. Ser.*, 656.
[12] J. Blake, 1987, *Annu. Rev. Fluid Mech.*, 19 (1), 99–123.
[13] I. Karathanassis, P. Koukouvinis, M. Gavaises, 2017, *Int. J. Multiph. Flow* 95, pp. 257–270.
[14] J.-P. Franc, J.-M. Michel, 2004, "Fundamentals of cavitation", Kluwer Academic Publishers.
[15] K. S. Suslick, 1990, *Science (80-.)*,247 (4949), pp. 1439–1445.
[16] E. P. Stride, C. C. Coussios, 2010, *Proc. Inst. Mech. Eng. Part H J. Eng. Med.*, 224 (2), 171–191.
[17] M. Chappell, S. Payne, 2006, *Respir. Physiol. Neurobiol.*, 153 (2), pp. 166–180.
[18] D. Cosgrove, 2006, *Eur. J. Radiol.* 60 (3), pp. 324–330.
[19] C. Pichon, K. Kaddur, P. Midoux, F. Tranquart, A. Bouakaz, 2008, *J. Exp. Nanosci.*, 3 (1), pp. 17–40.
[20] A. V. Alexandrov, 2006, *Int. J. Stroke*, 1 (1), pp. 26–29.
[21] J. L. Bull, 2007, *Expert Opin. Drug Deliv.* 4 (5), pp. 475–493.
[22] B. Cockburn, G. E. Karniadakis, C. W. Shu, 2000, *Lecture Notes in Computational Science and Engineering* (11), pp. 3–50.
[23] J. Ekaterinaris, 2005, *Progress in Aerospace Sciences*, 41 (3-4), 192–300.
[24] Z. J. Wang, 2007, *Prog. in Aerosp. Sciences*, 43 (1-3), 1–41.
[25] B. Cockburn, C.-W. Shu, 1998, *J. Comput. Phys.*, 141 (2), pp. 199–224.
[26] Y. Liu, M. Vinokur, Z. Wang, 2006, *J. Comput. Phys.*, 212 (2), pp. 454–472.
[27] Y. Liu, M. Vinokur, Z. Wang, 2006, *J. Comput. Phys.*, 216 (2), pp. 780–801.
[28] M. Yu, Z. Wang, Y. Liu, 2014, *J. Comput. Phys.*, 259 (15) pp. 70–95.
[29] J. Cheng, C. W. Shu, 2007, *J. Comput. Phys.*, 227 (2), pp. 567–1596.
[30] G. S. Jiang, C. W. Shu, 1996, *J. Comput. Phys.*, 126, pp. 202–228.
[31] P. Koukouvinis, M. Gavaises, A. Georgoulas, M. Marengo, 2015, *J. Phys. Conf. Ser.*, 656, pp. 012087.
[32] P. Koukouvinis, G. Strotos, Q. Zeng, S. R. Gonzalez-Avila, A. Theodorakakos, M. Gavaises, 2012, *Langmuir*, 34 (22), pp. 6428–6442.
[33] F. Örley, T. Trummler, S. Hickel, M. S. Mihatsch, S. J. Schmidt, N. A. Adams, 2015, *J. Phys. Conf. Ser.*, 656, pp. 012096.
[34] A. Morozov, U. Iben, 2008, HEFAT, Pretoria, South Africa.
[35] J. Qiu, T. Liu, B. C. Khoo, 2007, *J. Comput. Phys.*, 222 (1), pp. 353–373.
[36] Z. Jin, C. Yin, Y. Chen, H. Hua, 2017, *Ocean Eng.*, 130, pp. 597–610.
[37] R. P. Fedkiw, 2001, "Godunov Methods", Springer US, Boston, MA, pp. 309–317.
[38] v. d. J. Vegr, R. S., 2012, *J. Comput. Phys.*, 231, pp. 7564–7583.
[39] S. M. Schnepp, W. T., 2012, *J. App. and Comp. Math.*, 236, pp. 4909–4924.
[40] S. M. Schnepp, *J. App. and Comp. Math.*, 2014, pp. 353–368.
[41] M. A. Kopera, F. X. Giraldo, 2014, *J. Comput. Phys.*, 275, 92–117.
[42] A. Guittet, M. Theillard, F. Gibou, 2015, *J. Comput. Phys.* 292 (C), pp. 215–238.
[43] A. Papoutsakis, S. S. Sazhin, S. Begg, I. Danaila, F. Luddens, 2018, *J. Comput. Phys.*, 363, pp. 399–427.
[44] J. Anderson, 1995, "Computational Fluid Dynamics: The Basics with Applications", McGraw-Hill Education.
[45] J. Safarov, U. Ashurova, B. Ahmadov, E. Abdullayev, A. Shahverdiyev, E. Hassel, 2018, *Fuel*, 216, pp. 870 – 889.
[46] N. Kyriazis, Ph. Koukouvinis, M. Gavaises, 2018, *Adv. in Coll. and Interf. Sci.*, 260, pp. 46–64
[47] G. Karniadakis, S. Sherwin, 2003, "Spectral/hp Element Methods for CFD", Oxford University Press.
[48] E.F. Toro, 1990, "Riemann Solvers and Numerical Methods for Fluid Dynamics'.
[49] J. Zhu, J. Qiu, T. Liu, B. C. Khoo, 2011, *Appl. Numer. Math.*, 61 (4), pp. 554–580.
[50] W. Lauterborn, C. Lechner, M. Koch, R. Mettin, 2018, *IMA J. Appl. Math.*, 83 (4), pp. 566–589.
[51] M.R. Saleem, I. Ali, S. Qamar, 2018, *Results Phys.*, 8, pp. 379–390.
[52] K. Hejranfar, M. Hajihassanpour, 2017, *Comput. Fluids*, 156, pp. 175–199.
[53] F. Nicoud and F. Ducros, 1999, *Turbulence, and Combustion.*, 62(3), pp. 183–200.
[54] E. Lauer, X.Y. Hu,S. Hickel, N.A. Adams, 2012, *Comput. Fluids*, 69, pp. 1–19.
[55] H. Kobayashi, 2005, *Phys. Fluids*, 17(4), pp. 045104.
[56] S. Hickel, N.A. Adams, J.A. Domaradzki, 2006, *J. Comput. Phys.*, 213, pp. 413–436.